Indentation fracture of low-dielectric constant films: Part II. Indentation fracture mechanics model

Dylan J. Morris[a] and Robert F. Cook
Materials Science and Engineering Laboratory, National Institute of Standards and Technology, Gaithersburg, Maryland 20899-8520

(Received 5 February 2008; accepted 16 May 2008)

Part I [D.J. Morris and R.F. Cook, *J. Mater. Res.* **23,** 2429 (2008)] of this two-part work explored the instrumented indentation and fracture phenomena of compliant, low-dielectric constant (low-κ) films on silicon substrates. The effect of film thickness and probe acuity on the fracture response, as well as the apparent connection of this response to the perceived elastic modulus, were demonstrated. These results motivate the creation of a fracture model that incorporates all of these variables here in Part II. Indentation wedging is identified as the mechanism that drives radial fracture, and a correction is introduced that adjusts the wedging strength of the probe for the attenuating influence of the relatively stiff substrate. An estimate of the film fracture toughness can be made if there is an independent measurement of the film stress; if not, a critical film thickness for channel-cracking under the influence of film stress may be estimated.

I. INTRODUCTION

Part I of this work outlined some of the phenomena of radial crack initiation and propagation in low-dielectric constant (low-κ) films at contacts by sharp probes.[1] It was shown that the conventional analysis for estimation of fracture toughness by indentation is inapplicable due to the clear dependence of the indentation fracture response on the film thickness and the apparently complex crack-length–indentation-load scaling involved. Furthermore, one of the core physical assumptions of the conventional indentation fracture model (volume conserving plastic deformation) is likely broken for low-κ films, as the incorporation of porosity for low-dielectric constants will almost necessarily result in densification being the dominant irreversible deformation mode.

This paper develops concepts and a model that attempt to capture the important physics of the indentation fracture response of thin, porous films. With this, a method for the estimation of the fracture toughness of low-κ films is presented. Section II modifies the "wedging" radial crack development model of Morris and Cook[2] for the presence of a stiff, constraining substrate in two ways: by consideration of the constraint of the substrate on crack shape and on the attenuation of the indentation crack-driving stresses within the film by the substrate. Section III outlines the effect of pre-existing film stress on the fracture response. In Sec. IV, the complete fracture model is developed and compared with experimental data. Simulation of fracture responses in Sec. V shows the way that all three substrate effects (crack shape change, indentation stress attenuation, and film stresses) play a role in the fracture response.

II. INDENTATION CRACK DRIVING FORCES

A. Indentation stress-intensity factors for different crack shapes

Estimation of fracture properties in small volumes, or on samples ill-suited to conventional fracture-specimen preparation, requires a local mechanical property probe such as indentation. In most ceramics and glasses, the hoop-tensile residual stress field caused by the reaction of the plastically deformed zone just below a Vickers indentation impression drives fracture that extends radially from the impression center.[3] The stress-intensity factor (SIF) at the radial cracks after the indenter is unloaded is the residual SIF K^{R}:

$$K^{\mathrm{R}} = \chi^{\mathrm{R}} \frac{P}{c^{3/2}} \quad , \tag{1}$$

where P is the indentation load, c is the crack surface trace length, and χ^{R} is a semi-empirical stress-field amplitude:

$$\chi^{\mathrm{R}} = \xi^{\mathrm{R}} \left(\frac{E}{H}\right)^{1/2} \quad , \tag{2}$$

[a]Address all correspondence to this author.
e-mail: dylan.morris@nist.gov
DOI: 10.1557/JMR.2008.0295

where E is the elastic modulus, H is the indentation hardness, and ξ^R is a calibrated material-invariant (but indenter-geometry dependent) constant. Equation (2) may be derived by consideration of volume-conserving plastic flow underneath the indenter. Many ceramics and glasses (such as soda-lime glass) satisfy this requirement, and reasonable estimates of the fracture toughness, T, may be made on unknown brittle materials with Eqs. (1) and (2) and invocation of fracture equilibrium, $K^R = T$.[4]

The low-κ organosilicate materials in this work have a low-dielectric constant due to incorporation of porosity into what can be thought of as essentially amorphous silica. Amorphous silica glass (fused silica) is well known as a material that has an open structure.[5] The open structure in fused silica is responsible for the accommodation of permanent deformation at an indentation by densification instead of volume-conserving plastic flow[6,7]; this alternative plastic deformation mechanism greatly weakens the strength of χ^R and would lead one to overestimate the toughness of silica by Eq. (1). Since the toughness of bulk homogeneous fused silica cannot be estimated by the conventional indentation fracture model, it is extremely unlikely that any reliable toughness estimations could be made of low-κ materials, even if obtainable in bulk form, with a Vickers indenter.

Fortunately, recent work has shown that radial crack evolution for the much more acute cube-corner indenter geometry is dominated by the elastic field of the probe,[8,9] which is composed of two parts: an elastic contact (flat-punch like) component and a "wedging" component. The wedging stress field is so named because it pries open the radial cracks only when the indenter is in contact. The residual elastic-plastic field could be ignored in describing the evolution of radial cracks for the cube-corner geometry, even for soda-lime glass. The elastic-contact and wedging stress fields are insensitive to plastic deformation mechanisms, which explains why the fracture behavior of fused silica and soda-lime glass is so similar for cube-corner indentation[10,11] but different for indentation by the much less acute (and consequently poor wedge) Vickers or Berkovich indenters. Therefore, the indentation wedging model of Morris and Cook[11] for radial crack propagation and stabilization will be used in this work.

One consequence of the dominant wedging mechanism of the cube-corner is that after the indenter has been unloaded, the indentation driving force for cracking has disappeared, in contrast to the residual elastic-plastic mechanism. What is observed after the indentation event is the metastably trapped (unhealed) crack, and so the problem is to estimate the maximum indentation SIFs that were attained in the indentation cycle. The experimental evidence is that the point of maximum SIF happens sometime between peak load and complete unload.[11] While crack growth during loading to peak load is believed to be well understood, the crack growth during unloading, so far, has not been modeled precisely.[2,9] Experimentally, however, it is found that the maximum crack length is nearly attained at peak load; during unloading, there is no more than 10% crack extension.[11] Therefore, for tractability of the current problem, it is assumed that the cracks reached their final shape at peak indentation load.

Figure 1(a) is a representative scanning-electron micrograph (SEM) of a cube-corner indentation on a low-κ film. From micrographs such as this, the impression

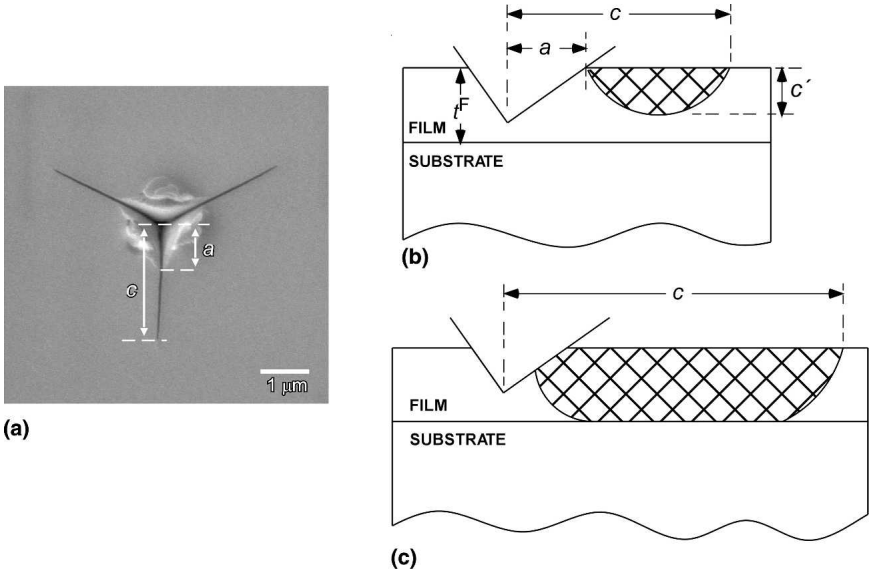

FIG. 1. (a) Scanning electron image of a cube-corner indentation on a low-κ film with the contact dimension a and surface crack length c defined. (b) Schematic cross-sectional diagram of a partially cracked film; the crack depth c', film thickness t^F, and a and c are defined. (c) Schematic cross-sectional diagram of a one-dimensional channel crack with surface crack length c.

center-to-corner distance a and surface crack length c may be measured. Figure 1(b) is a cross-sectional schematic diagram of the crack geometry expected at the smallest indentation loads; that is, when the radial cracks are contained well within the film and any subsequent crack extension may occur down toward the substrate and away from the axis of indentation. The impression center-to-corner distance a, crack length c and subsurface crack depth are shown on Fig. 1(b). The SIFs at load P for the wedging and elastic-contact stress fields in a homogeneous material are[2]

$$K_{PC}^{W} = \chi_{PC}^{W} \frac{P}{c^{3/2}} \quad , \tag{3}$$

$$K_{PC}^{E} = \chi_{PC}^{E} \frac{P}{c^{3/2}} \ln(2c/a) \quad , \tag{4}$$

where χ^{W} and χ^{E} are semi-empirical amplitude terms relating stress-intensity factors to probe acuity and the Poisson's ratio ν of the material. The subscript PC (partially cracked, referring to the depth of the radial cracks in the film) has been appended to the stress-intensity factors and stress-intensity factor amplitudes. Equations (3) and (4) can be derived by approximating the radial cracking system as a circular crack with a radially symmetric stress distribution of the type $1/r^3$ for the wedging stress field and $1/r^2$ for the elastic-contact stress field.[2]

The presence of a stiff, tough substrate, normally silicon for low-κ films, is a severe constraint on the shape evolution of radial cracks that is not present in a homogeneous material. This constraint can give rise to two fundamentally different crack geometries when radial cracks are contained within the low-κ film and delamination has been avoided at or near the interface: that of the partially cracked film, and that of the fully cracked film. Figure 1(c) is a schematic diagram of the fully cracked film, or channeling-crack, geometry; the crack is constrained by the tougher, stiffer substrate and may only extend in one dimension—outward through the film.

A channeling-cracked film differs from the homogeneous material or partially cracked film primarily by the loss of a characteristic crack dimension, and so the simplest way to account for this change in crack geometry is to approximate the channel crack as a straight-fronted one-dimensional crack. The weighting function SIF expression for a stress distribution acting over a one-dimensional crack is[12]

$$K = \frac{2}{\pi^{1/2}} c^{1/2} \int_a^c \frac{\sigma(r)}{(c^2 - r^2)^{1/2}} \, dr \quad , \tag{5}$$

where r is the radial coordinate, and the edge of the contact zone a is chosen as the inner boundary of the crack. The characteristic stress distributions ($1/r^3$ and $1/r^2$ for wedging and elastic-contact, respectively) are substituted into Eq. (5) to derive the forms for the one-dimensional (channeling) crack:

$$K_{CH}^{W} = \chi_{CH}^{W} \frac{P}{c^{3/2}} \left[\frac{c}{a} + \frac{a}{c} \ln(2c/a) \right] \quad , \tag{6}$$

$$K_{CH}^{E} = \chi_{CH}^{E} \frac{P}{c^{3/2}} \left[\frac{c}{a} \right] \quad . \tag{7}$$

(The approximation $c^2 \gg a^2$ has been used to arrive at all of these SIFs.) The subscript CH denotes application to channeling cracks. All four indentation-derived stress-intensity factors [Eqs. (3), (4), (6), and (7)] retain an essential $P/c^{3/2}$ character with modifications by a dimensionless function of c/a. Both χ_{CH} values are expected to be of the same magnitude as, but not equal to, that of χ_{PC}. This is explored further in Sec. IV.

B. Substrate attenuation

A common problem in nanoindentation is measurement of the plane-strain modulus, $\bar{E} = E/(1 - \nu^2)$ of thin films, where E is Young's Modulus. It is frequently difficult, even with the most sensitive instruments, to perform an experiment that is assured to sense the plane-strain modulus of the thin film, $\bar{E}^{F}$, alone. The apparent plane-strain modulus $\bar{E}^{A}$ (the perceived modulus from appropriate interpretation of the indentation experiment) will differ from $\bar{E}^{F}$ at any finite indentation depth. A robust experimental approach is to perform the indentations over a range of depths and then to extrapolate $\bar{E}^{A}$ to an indentation depth of zero via an appropriate contact mechanics model.[13–16]

In the companion paper,[1] the Xu–Pharr model[14] for indentation of a coated substrate was simplified to the case of a compliant film $\bar{E}^{F} = \bar{E}^{S}$ to yield the relation

$$\bar{E}^{A} = \bar{E}^{F}/I_0 \quad . \tag{8}$$

I_0, the fraction of the total indentation strain energy contained in the film, is a unique function of the contact-radius-to-film-thickness ratio a/t^{F}. The (somewhat complex) expression for I_0 is derived in Gao et al.[13] and reproduced in Part I.[1] Remarkably, Eq. (8), with only one adjustable parameter ($\bar{E}^{F}$), was able to describe the composite indentation elastic response of all four low-κ film–silicon substrate systems listed in Table I. In the context

TABLE I. Properties of low-dielectric constant materials.

Material	κ	t^{F} (μm)	σ^{F} (MPa)	H^{F} (GPa)	$\bar{E}^{F}$ (GPa)
LKA	2.8	2.0, 1.5, 1.0, 0.5	58.2, 61.2, 63.6, ⋯	1.5	9.3
LKB	2.2	2.4, 1.6, 1.2	⋯	0.4	3.1
LKC-1	2.4	1.0	⋯	0.5	3.8
LKC-2	2.0	1.0	⋯	0.2	1.8

of the indentation fracture model developed in this work, finding an accurate extrapolative form for $\bar{E}^{A}$ data is not the primary concern. The utility of Eq. (8) is that it allows us to connect measurable quantities, $\bar{E}^{A}$ and $\bar{E}^{F}$, to the proportion of indentation strain energy lost to the substrate.

The indentation SIFs implicitly assume that a homogeneous material is being indented, and therefore the crack-driving stress fields at the material surface are self-similar with respect to the load on the punch. This cannot be the case when indenting a film that is elastically mismatched to a substrate. By strain compatibility at a film-substrate interface, the stresses outside the contacted area in an infinitely thin ($a \gg t^{F}$) bonded film are reduced (for a compliant film) from the surface stresses in the substrate by a factor of $\bar{E}^{F}/\bar{E}^{S}$. Of course, in this case, the indentation strain energy is almost entirely contained in the substrate ($I_0 \to 0$). Conversely, when $a \ll t^{F}$, the mechanical response is that of the film only, $I_0 \to 1$, and the indentation stresses in the film are unaffected by the substrate. In between these two limiting cases, there will be some reduction in the magnitude of the stresses in the film from those occurring at a modulus-matched film–substrate system.

Therefore, some correction is needed for the wedging and elastic contact stresses (and by extension, the indentation stress-intensity factor amplitudes) for the radial cracks in the film. Compensation for the stress-attenuating influence of the substrate is made by weighting the indentation SIFs linearly by the fraction of strain energy in the film I_0, which is experimentally estimable as the $\bar{E}^{F}/\bar{E}^{A}$ ratio. A better, or "true" SIF weighting need not be linear in I_0, but the linear assumption appears to work well at this stage. The effect of substrate attenuation on the film fracture response is discussed in Sec. V.

III. FILM-STRESS CRACK DRIVING FORCES

A. Partially cracked film

Many low-κ films have a preexisting tensile stress σ^{F} at room temperature, providing an additional driving force for crack propagation. In this work, the film-fracture results of Beuth are used to estimate the contribution of the pre-existing film stresses on the overall fracture response.[17] Results were presented over a wide range of elastic mismatch between film and substrate, compactly represented by the bi-material plane-strain Dundurs parameters, α and β:

$$\alpha = \frac{\bar{E}^{F} - \bar{E}^{S}}{\bar{E}^{F} + \bar{E}^{S}} \quad , \tag{9}$$

$$\beta = \frac{\mu^{F}(1 - 2\nu^{S}) - \mu^{S}(1 - 2\nu^{F})}{2\mu^{F}(1 - \nu^{S}) + 2\mu^{S}(1 - \nu^{F})} \quad , \tag{10}$$

where μ is the shear modulus, and superscripts F and S refer to the film and substrate, respectively. α as defined is −1 when the substrate is rigid, a good approximation for low-κ materials on silicon. Numerical results for the SIF of a plane-strain surface crack propagating toward the interface of depth $c' \leq t^{F}$ were represented with the approximate formula:

$$K_{PC}^{F} = 1.1215\sigma^{F}(\pi t^{F})^{1/2}\left(\frac{c'}{t^{F}}\right)^{1/2} \left(1 - \frac{c'}{t^{F}}\right)^{1/2-s}\left(1 - \lambda\,\frac{c'}{t^{F}}\right) \quad , \tag{11}$$

where λ is a tabulated function of α for $\beta = 0$ and $\beta = \alpha/4$ that improves the quality of fit between Eq. (11) and the numerical SIF results near $c' = t^{F}$, and s is the Zak–Williams stress-singularity exponent.[18,19]

The Zak–Williams stress-singularity exponent arises from consideration of the stresses ahead of a crack tip located precisely at, and perpendicular to, a bi-material interface. The stress field about the crack tip in a homogenous material is singular at the crack tip; no matter what the details of the outer loading of the cracked body are, the stress singularity is of strength $r^{-1/2}$.[3] However, in the Zak–Williams problem, the crack-tip singularity will have a strength of r^{-s}. s is a function of the Dundurs parameters only and satisfies

$$\cos(s\pi) - 2\,\frac{\alpha - \beta}{1 - \beta}\,(1 - s^{2}) + \frac{\alpha - \beta^{2}}{1 - \beta^{2}} = 0 \quad . \tag{12}$$

It is easily verified that when $(\alpha, \beta) = 0$, $s = 0.5$, which is the usual strength of the crack-tip stress singularity in a homogeneous stressed body. It should be made clear that the crack-tip singularity is r^{-s} only at that instant the crack-tip is at the interface; when the crack tip is in either material, the stress singularity is still $r^{-1/2}$. The physical significance of s in Eq. (11) is to embed elastic mismatch information (and identify which material is cracked) into the SIF.

Frequently in discussions of bi-material elastic problems, physically admissible conditions are set such that $\mu > 0$ and $0 \leq \nu \leq 1/2$, and all possible combinations of material parameters are contained within a parallelogram in the α, β plane defined by $|\alpha - 4\beta| \leq 1$.[19,20] Like Beuth's results, many published results for bi-material fracture problems primarily explore the influence of α, while limiting β to the range $0 < \beta < \alpha/4$.[17,21] This is because β is thought to be of secondary importance to α for most bi-material elasticity solutions[19]; furthermore, a survey of practical composite material combinations showed that nearly all composite materials fell into the

range $0 < \beta < \alpha/4$ while spanning the entire range of α.[22] However, as argued below, low-κ films on silicon substrates will likely fall well outside of $0 < \beta < \alpha/4$, and the fracture behavior will in fact be sensitive to β. Furthermore, β depends most strongly on the unknown Poisson's ratio of the cracked film.

Lucas et al.[23] have shown with novel three-dimensional indentation experiments that good estimates of Poisson's ratio could be made on known materials by measuring the ratio of normal to tangential stiffness. Further experiments on polymeric low-κ films[24] showed that there was a demonstrable relationship between porosity and ν; the perceived Poisson's ratio of the low-κ materials varied from about $\nu = 0.4$ for a fully dense film to $\nu = -0.05$ for an identical precursor material that had a starting incorporated porogen content of 50%. For silicate-based low-κ materials, the probability that the Poisson's ratio is small is even greater. The fully dense analogue to organosilicate low-κ materials, fused silica, has a Poisson's ratio of only $\nu = 0.18$. Unoccupied volume in the structure is a crucial component of small Poisson's ratio materials, and mechanisms have been identified specifically in certain foam materials[25,26] and silicates[27] that contribute to auxetic (negative Poisson's ratio) behavior. It is likely that Poisson's ratio is in the neighborhood $\nu^F \cong 0$ for the silicate low-κ materials used in this study.

Although auxetic materials are rare, it is pointed out here that all $-1 > \nu > 0.5$ are thermodynamically admissible for isotropic, continuous, elastic media,[28,29] and therefore the Dundurs parameters should really be subject to the restriction $|\alpha - 8\beta/3| \leqslant 1$. Figure 2 shows the bounding parallelogram in the α, β plane. The top and bottom bounding lines correspond to extreme mismatch in Poisson's ratio, while the bounds on α correspond to extreme mismatch in plane-strain modulus. In fact, any line crossing the α, β plane from $\alpha = (+1, -1)$ is fixed at its ends by the Poisson's ratio of the (stiff, compliant) material. The physical significance of lines and other geometric constructions in the α, β plane was discussed much more completely by Dundurs.[20] Also drawn in Fig. 2 are the lines $\beta = 0$ (ν^F, $\nu^S = 1/2$) and $\beta = \alpha/4$ (ν^F, $\nu^S = 1/3$), which correspond to the frequently cited limits for typical material combinations. Therefore, in the rigid substrate limit ($\alpha = -1$), β falls outside of the typical bounds of 0 and $\alpha/4$ if ν^F is smaller than 1/3.

Figure 3 is a map of s according to Eq. (12) in the α, β plane within the bounding parallelogram. Lines of constant s all coincide at (1, −1). For large α, s is primarily a function of α, while at small α, s is primarily a function of β. It is seen that s is small and changes rapidly in the vicinity of $\alpha = -1$ and $\beta = -0.5$. This makes it clear that the SIF of the cracked low-κ film [by Eq. (11)] depends crucially on the Poisson's ratio of the film. This is not true for a cracked, relatively stiff film; s is insensitive to Poisson's ratio as $\alpha \to 1$. The shaded area in the lower-left corner is a region where Eq. (12) has no root in the range $0 \leqslant s \leqslant 1$. In fact, in this region Eq. (12) may have no roots at all, or one or more negative roots, and the physical significance of s here is not clear. Particular to the low-κ film systems studied in this work, Fig. 4 is a map of s as a function of film elastic modulus E^F and film Poisson's ratio ν^F, assuming the film is on a ⟨100⟩-oriented Si substrate (with $E^{Si} = 165$ GPa and $\nu^{Si} = 0.18$[30]).

If, in fact, we have a low-Poisson's ratio film on a comparatively stiff substrate, s corresponding to that material combination will be much different than the elastic mismatches that Beuth considered explicitly. A reasonable estimate of K^F_{PC} can be made by Eq. (11) with $\lambda = 0$,[17] and this approximation is necessary for extrapolation of Beuth's results to the small s regime. Therefore, the form of K^F_{PC} used in this work for the partially cracked film SIF is

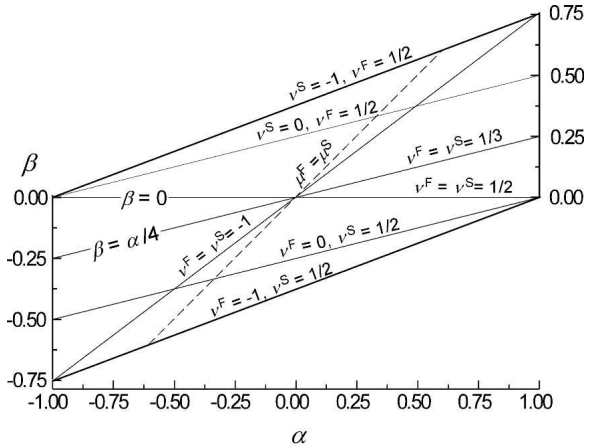

FIG. 2. α, β plane with the parallelogram defined by $|\alpha - 8\beta/3| \leqslant 1$ bounding the physically admissible isotropic elastic constants.

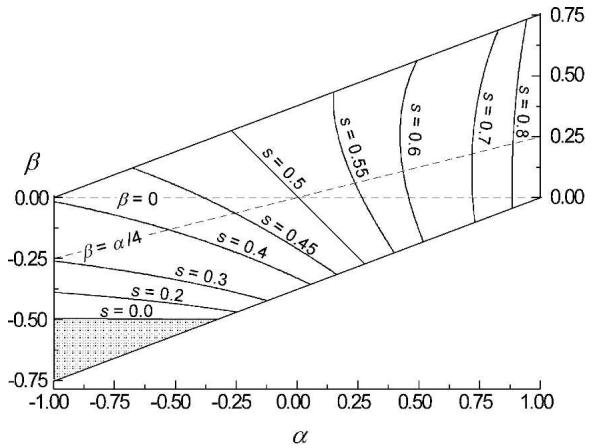

FIG. 3. Map of the Zak–Williams stress-singularity exponent s on the α, β plane in the parallelogram defined by $|\alpha - 8\beta/3| \leqslant 1$.

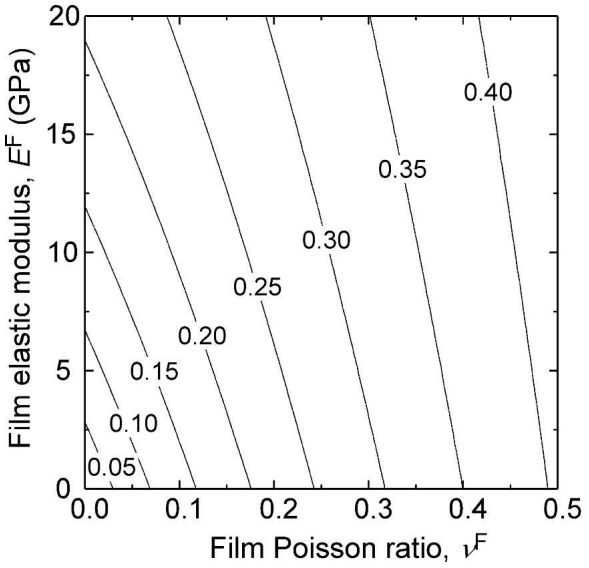

FIG. 4. Map of Zak–Williams stress singularity exponent s as a function of film elastic modulus and film Poisson's ratio, assuming the film is on a silicon substrate (E^{Si} = 165 GPa, ν^{Si} = 0.17).

$$K_{PC}^{F} = 1.987\sigma^{F}(t^{F})^{1/2}\left(\frac{c'}{t^{F}}\right)^{1/2}\left(1-\frac{c'}{t^{F}}\right)^{1/2-s} \quad . \qquad (13)$$

Within the approximate stress-intensity factor of Eq. (13), all four independent elastic constants of the bimaterial problem have been mapped on to s. Figure 5 is a plot of a normalized SIF, $K_{PC}^{F}/\sigma^{F}(\pi t^{F})^{1/2}$, as a function of normalized crack depth, for various values of $0 \leqslant s \leqslant ½$, appropriate for a compliant film. Any $s < ½$ will reduce K_{PC}^{F} below that of the isotropic SIF at all crack depths and eventually drive K_{PC}^{F} to zero as the crack approaches the interface. The maximum in K_{PC}^{F}, by Eq. (13), is at $c' = -1/2(s-1)$. As s approaches zero ($\bar{E}_S \to \infty$ and $\nu_F \to 0$), the maximum in K_{PC}^{F} tends to the midpoint of the film. Obviously, from Fig. 5, crack propagation through a compliant, low-ν film [as expressed by s, Fig. 3(b)] is markedly different from an elastically matched film. The SIF field for cracked auxetic films might be distorted even further, but this is not explored in this work.

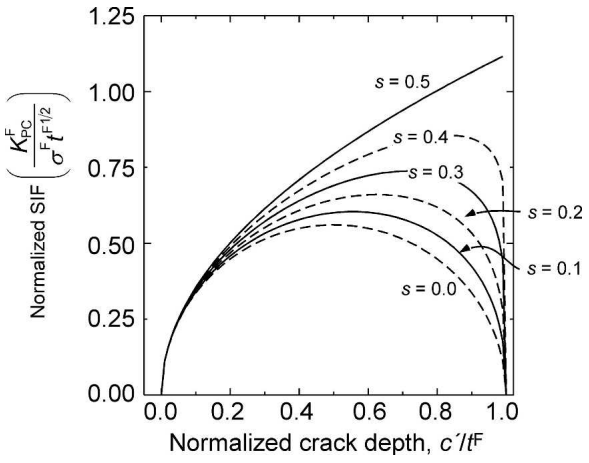

FIG. 5. Normalized stress-intensity factor as a function of normalized crack depth in a compliant film. When s = ½, the result for a surface-located plane-strain crack is recovered, $K \propto c'^{1/2}$. $s < ½$ distorts the stress-intensity factor field and drives the stress-intensity factor to zero as the crack tip approaches the film-substrate interface at $c'/t^F = 1$.

B. Channeling-cracked film

When the propagation of the crack toward the interface is sufficiently constrained by the tough substrate, the radial crack loses two-dimensional character and becomes a one-dimensional crack—a channeling crack. The appropriate SIF from film stress is

$$K_{CH}^{F} = \psi_{CH}(\alpha,\beta,c'/t^{F})\sigma^{F}(t^{F})^{1/2} \quad . \qquad (14)$$

K_{CH}^{F} is a neutral stress-intensity factor; that is, there is no surface crack-length dependence. The channeling geometry factor ψ_{CH} is derived from K_{PC}^{F} by averaging the mechanical energy release rate $G = K^2/E^F$ of a partially cracked film extending toward the interface to a depth c' through[17]

$$G_{CH} = \frac{1}{c'}\int_0^{c'} G_{PC}\, dc' \quad . \qquad (15)$$

It is emphasized that "sufficient constraint" is chosen as the condition for the transition from partially cracked to channeling-crack geometries, and not the actual meeting of the radial crack edge with the film–substrate interface. In a compliant film under the influence of the film stress alone, the channeling crack will arrest stably some distance from the interface because K_{PC}^{F} tends to zero at the interface (see Fig. 5). This has been observed experimentally.[31] Figure 6 is a plot of ψ_{CH} for various values of s as a function of channeling depth. The usual assumption is that the channeling crack has a depth identical to the film thickness, such that $c' = t^F$ is a good approximation for the steady-state channeling crack depth. For $s = 0$ (the most severe test of this assumption), there is only a 6% difference between the maximum ψ_{CH} (which is at $c' = 3/4t^F$) and ψ_{CH} for the fully cracked film ($c' = t^F$). Therefore, while it is not necessary, or even probable, for the crack to reach the interface to attain a channeling geometry, it is a good assumption that the crack has reached the interface for purposes of estimating ψ_{CH}. Figure 7 is a plot of ψ_{CH} calculated with Eq. (13) for $c' = t^F$ as a function of s. The channeling geometry factor varies from the homogeneous-material limit ψ_{CH} = 1.41 at s = ½ to ψ_{CH} = 0.81 at s = 0.

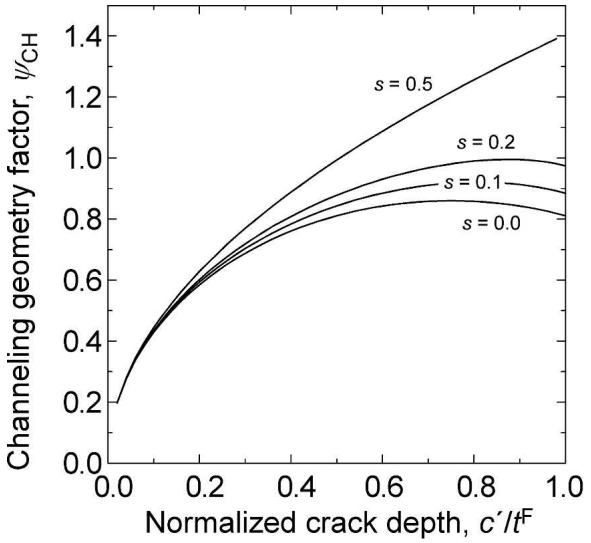

FIG. 6. Channeling-crack geometry factor ψ_{CH} as a function of normalized channel crack depth for values of s between 0.5 (no elastic mismatch) and 0.0 (rigid substrate, $\nu^F = 0.0$). For $s < 0.5$, a maximum ψ_{CH} corresponds to a channeling depth less than the film thickness.

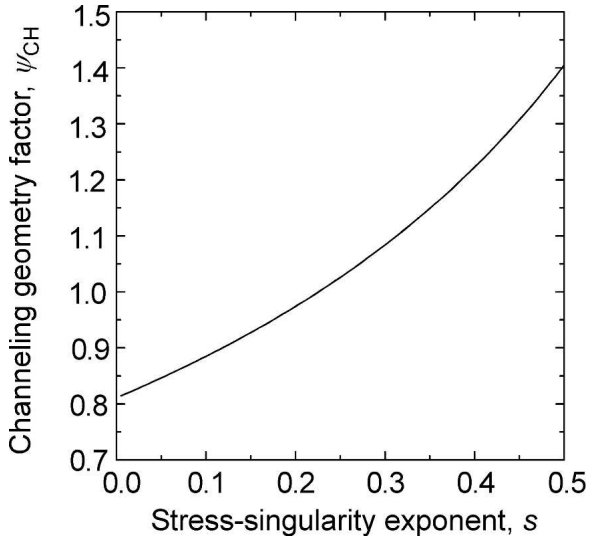

FIG. 7. ψ_{CH} as a function of stress-singularity exponent s for a fully cracked film ($c' = t^F$), calculated using the expression for K^F_{PC} in Eq. (13).

IV. APPLICATION TO EXPERIMENTAL DATA

A. Complete fracture model

To estimate the fracture toughness of the film, we must estimate the contribution of all of the SIFs, add them, and set them equal and opposite to the fracture toughness of the film; this is a statement of fracture equilibrium. It is further assumed that the toughness of the film is insensitive to crack length; that is, there is no *R*-curve behavior. This is likely a good assumption for an amorphous, brittle material. The fracture equilibrium relationship may then be rearranged as

$$K^W + K^E = T - K^F \quad . \tag{16}$$

The left side of Eq. (16) is interpreted as the total driving force for fracture introduced by the action of the indenting probe ($K^W + K^E$), and the right side as a composite resistance to fracture (but not strictly a "fracture resistance") caused by the material properties and configuration, which are the film thickness and residual stress derived from its attachment to a substrate.

As a practical matter, only the surface dimension of the radial cracks c can be measured conveniently (for example, in a conventional SEM or scanning-probe experiment). It is assumed from this point that when the film is partially cracked, the radial cracks have a constant aspect ratio ℓ such that $c' = \ell c$. With this assumption, the indentation SIFs, which call for c, and the film-stress SIFs, which call for c', may be added. For data-fitting purposes, the crack aspect ratio ℓ will normally be a free parameter.

The wedging fracture SIF amplitudes, χ^E and χ^W, are strong functions of the indenter acuity and the material Poisson's ratio.[2] This could be problematic because the Poisson's ratios of the low-κ films are unknown. However, it was also shown that the ratio of these SIF amplitudes is insensitive to Poisson's ratio, especially as $\nu \to 0$. This ratio is the probe wedginess, $W = -\chi^W/\chi^E$, a measure of the relative flat-punch to wedgelike character of a punch of fixed acuity. The cube-corner has an observed wedginess of approximately 1.95.[11] By way of example, the predicted wedginesses of the 49.6°, 58.9°, and Berkovich probes (at $\nu = 0.0$) are 1.56, 1.07, and 0.70, respectively; and of course, a flat punch would have no wedgelike character, $W = 0$. Here only cube-corner results are analyzed because wedginess has been experimentally measured for such a probe. W depends to first order only on probe geometry, and so the equilibrium relationship for a partially cracked film may be rewritten, by substitution of equations, as

$$\frac{\bar{E}^F}{\bar{E}^A}\left[K'^W_{PC}W - \frac{1}{W}K'^F_{PC}\right] = \left(\frac{T^F}{\chi^W_{PC}}\right) - 1.987\left(\frac{\sigma^F}{\chi^W_{PC}}\right)(t^F)^{1/2}\left(\frac{\ell c}{t^F}\right)^{1/2}\left(1 - \frac{\ell c}{t^F}\right)^{1/2-s}, \tag{17}$$

where the K' values are "dry" stress-intensity factors—SIFs from Eqs. (3) and (4) without any material-derived SIF amplitudes (χ) ascribed to them. The left side of Eq. (17) is a varying function of c only. Analogously, the channeling crack fracture relationship is rewritten as

$$\frac{\bar{E}^{F}}{\bar{E}^{A}}\left[K'^{W}_{CH}-\frac{1}{W}K'^{E}_{CH}\right]=\frac{1}{\omega}\left[\left(\frac{T}{\chi^{W}_{PC}}\right)-\psi_{PC}\left(\frac{\sigma^{F}}{\chi^{W}_{PC}}\right)(t^{F})^{1/2}\right] \quad , \tag{18}$$

where ω is an empirical constant such that $\chi_{CH} = \omega\chi_{PC}$ to compensate for the change in crack geometry. The left side of Eq. (18) has no dependence on crack length. The advantage of rewriting the film fracture equilibrium relationship in the manner of Eqs. (17) and (18) is that χ_{PC} (and ω) need not be known to make estimates of T^F if the film stress is known, by elimination of χ^W_{PC} between the quantities T^F/χ^W_{FC} and σ^F/χ^W_{PC}.

In Part I, it was shown that either a "jump" in the *c*-*P* response, or a sudden, sharp increase in $\bar{E}^A$ was a signal that a delamination crack was forming, and that the surface traces of the cracks may not be representative of true radial fracture. Where either of these conditions were met, the fracture data at and above that indentation load were discarded.

B. Results

For convenience, the names and properties of the films analyzed with the fracture model are reproduced from the companion paper in Table I.[1] They are designated by generic names of LK ("low-κ") A, B, and C. Each low-κ material, and its SEMATECH-reported film thickness and film stress (measured by wafer-curvature methods), indentation modulus $\bar{E}^F$ and hardness H^F as determined from Berkovich indentation is listed. Each low-κ material is coated on a silicon substrate. All three low-κ varieties are organosilicate; LKA ($\kappa \simeq 2.8$) is a chemical-vapor deposited material, while LKB ($\kappa \simeq 2.2$), LKC-1 ($\kappa \simeq 2.4$), and LKC-2 ($\kappa \simeq 2.0$) are spin-on methyl-silsesquioxane-based materials. More details about these materials and the indentation and fracture experiments are available in the companion paper.[1]

Figure 8 is a $c - \bar{E}^A - P$ plot for cube-corner fracture on 2.0-μm-thick LKA. This type of plot was used in Part I to deduce the transition from radial fracture to subsurface delamination. The crack length, load, and apparent modulus information in this type of plot may be transformed into the fracture mechanics variables of Eqs. (17) and (18) for plotting and data fitting, with the purpose of estimating T^F. To estimate *s*, the Poisson's ratio of all films was approximated as $\nu^F = 0$. This approximation is justified by the argument made in Sec. III. A; that is to say, a porous derivative of amorphous silica is likely to have a small Poisson's ratio. Then, *s* was found with Fig. 4 and the indentation modulus of the film (Table I).

Figures 9(a)–9(d) are plots of the indentation fracture SIFs, $\bar{E}^F/\bar{E}^A(K^W_{PC} - K^E_{PC}/W)$ and $\bar{E}^F/\bar{E}^A(K^W_{CH} - K^E_{CH}/W)$,

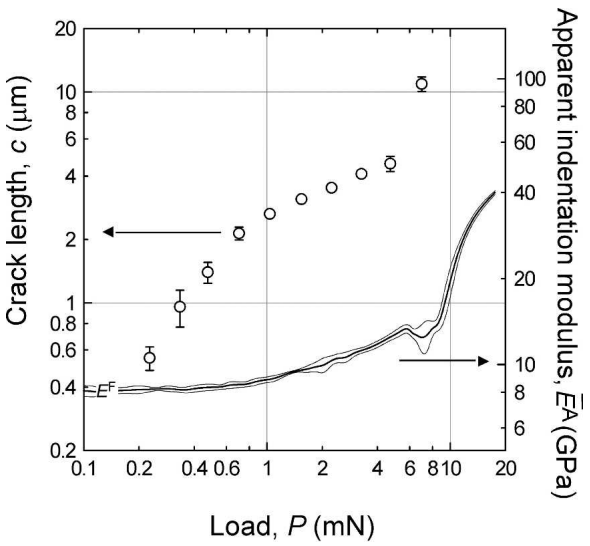

FIG. 8. A $c - \bar{E}^A - P$ plot for cube-corner indentation on 2.0-μm-thick LKA.

as a function of *c* for cube-corner indentation on 2.0-, 1.5-, 1.0-, and 0.5-μm LKA, respectively. (These data are transformed accordingly from data in Figs. 12–15, Part I[1]). All crack length data are plotted using partially cracked and fullycracked film models; we cannot determine a priori from surface crack lengths which cracks are of which type, but we can reasonably assume that the smallest cracks are best described by the former and the longest cracks by the latter. Finite element simulations have suggested that a channel crack under the influence of film stress reaches a steady state after it reaches a surface length twice the film thickness.[32]

The fitting and analysis procedure was as follows. Partially cracked fracture data up to $c = 1.5\,t^F$ were fit to Eq. (17) by Levenberg–Marquardt least-squares minimization. The least-squares residuals were weighted by $w_i = 1/\sigma_i^2$, where σ_i is the experimentally determined standard deviation (shown on the plot as error bars). All data for a particular material were fit simultaneously; T^F/χ^W_{PC} and *s* were shared for all data, while σ^F/χ^W_{PC} and ℓ were allowed to vary for individual film thicknesses. The quantities T^F/χ^W_{PC} and σ^F/χ^W_{PC} derived from the best fit, as well as ℓ and *s*, are listed in Table II. Uncertainty bands listed in Table II correspond to the uncertainty derived from the fitting procedure.

After the short-crack-length data were fit, channel-cracking data greater than $c = 1.5\,t^F$ were fit to Eq. (18), shown as a dashed line. Then from this, the constant ω was found by substitution of T^F/χ^W_{PC} and σ^F/χ^W_{PC} into Eq. (18). Values of ω are listed in Table II. The associated uncertainties were found by propagation of the uncertainties from the fit, and from T^F/χ^W_{PC} and σ^F/χ^W_{PC}.

As film thickness decreases, the decreasing importance of the film SIF on the total fracture response is

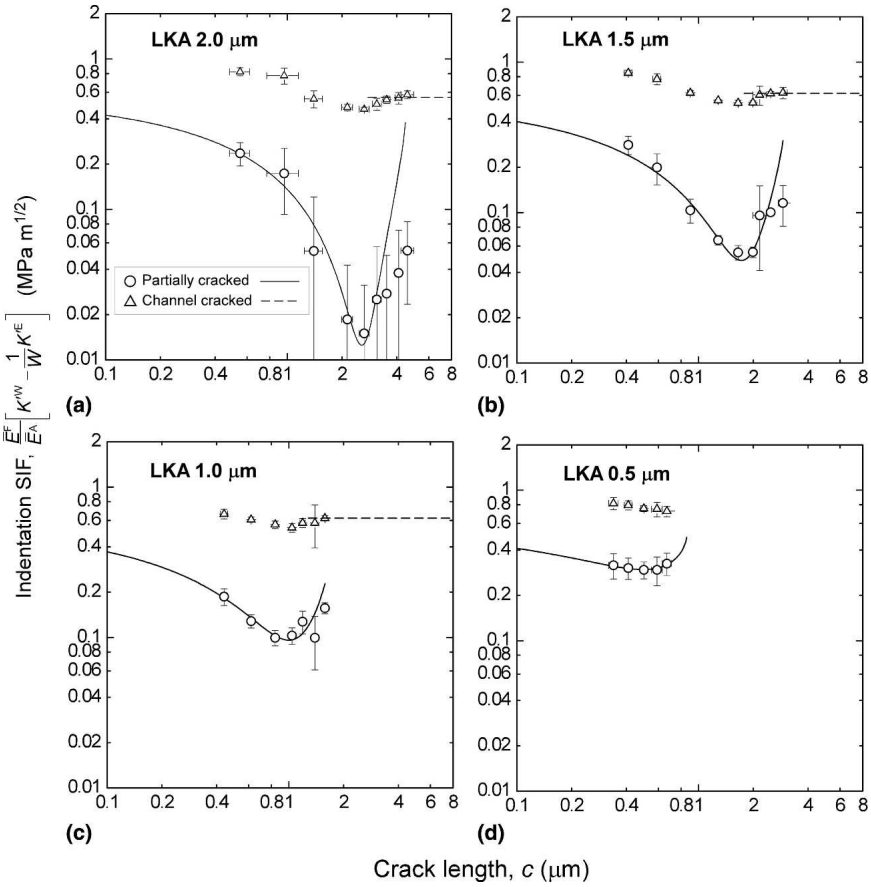

FIG. 9. Indentation stress-intensity factor for partially cracked films and channel-cracked films as a function of surface crack length for cube-corner fracture on (a) 2.0-μm-thick LKA, (b) 1.5-μm-thick LKA, (c) 1.0-μm-thick LKA, and (d) 0.5-μm-thick LKA. Fits of the respective film fracture models for each set of data are shown.

TABLE II. Low-κ film indentation fracture fitting results.

Material	t^F (μm)	T/χ^W_{PC} (MPa m$^{1/2}$)	σ^F/χ^W_{PC} (MPa)	ℓ	s	ω
LKA	2.0	0.58 ± 0.06	366 ± 42	0.44 ± 0.05	0.12	0.20 ± 0.15
	1.5		395 ± 47	0.50 ± 0.01		0.23 ± 0.13
	1.0		440 ± 59	0.57 ± 0.03		0.30 ± 0.13
	0.5		361 ± 87	0.58 ± 0.15		⋯
LKB	2.4	0.25 ± 0.01	145 ± 6	0.48 ± 0.02	0.05	0.28 ± 0.06
	1.6		154 ± 8	0.42 ± 0.03		⋯
	1.2		189 ± 8	0.44 ± 0.02		0.38 ± 0.06
LKC-1	1.0	0.25 ± 0.07	217 ± 76	0.40 ± 0.06	0.06	0.28 ± 0.42
LKC-2	1.0	0.22 ± 0.07	189 ± 68	0.50 ± 0.01	0.02	⋯

easily seen as an increase in the values of $\bar{E}^F/\bar{E}^A(K^W_{PC} - K^E_{PC}/W)$ across the entire crack length range as film thickness decreases. Furthermore, thicker films promote channel cracking. For example, the 0.5-μm-LKA film never achieved the channeling geometry before delamination occurred.

Figure 10(a) is a plot of the indentation fracture SIFs as a function of c for cube-corner indentation on 2.4-μm-thick LKB. The value of T^F/χ^W_{PC} found from the 2.4-μm LKB film was fixed when fitting the partially cracked 1.6- and 1.2-μm LKB films. Table II demonstrates that the apparent film stress, σ^F/χ^W_{PC} increases significantly as film thickness decreases, from σ^F/χ^W_{PC} in the 2.4-μm film to 189 MPa as the film thickness halves to 1.2 μm. The indentation fracture SIFs for 1.2-μm LKB are plotted in Fig. 10(b). In both LKA and LKB, the film stress appears to decrease with increasing film thickness. Measured film stresses (Table I) also increase with decreasing film thickness, but in smaller proportions than the fracture model suggests.

TABLE III. Calculated critical low-κ film thicknesses.

Film	t^F (μm)	ψ_{CH}	t^F_{crit} (μm)
LKA	2.0	0.90	3.1 ± 0.9
	1.5		2.6 ± 0.8
	1.0		2.1 ± 0.7
	0.5		3.1 ± 1.7
LKB	2.4	0.85	4.2 ± 0.5
	1.6		3.7 ± 0.5
	1.2		2.5 ± 0.3
LKC-1	1.0	0.87	1.8 ± 1.7
LKC-2	1.0	0.82	2.1 ± 2.0

The perceived increase in film stress with decreasing film thickness could be an artifact of the indentation fracture model, but it is probably not an artifact due to stress-corrosion cracking after the indentation. Thicker films (with equal stress) will have more available strain energy and so would tend to have artificially inflated crack lengths and therefore a higher perceived stress; this is the opposite of what is observed here. Stress variations in nominally similar films may be attributed to normal processing variability, or to relaxation of stress due to diffusion of water into the film.[33] At this time, the exact cause is not known.

Figure 10(c) plots the indentation fracture SIFs as a function of c for cube-corner indentation on 1.0-μm-thick LKC-1. As mentioned in Part I, the difference between LKC-1 and LKC-2 is the starting porogen content of the material before processing, which controls the final dielectric constant of the material after processing. It is interesting that the LKC materials have much more uncertainty in σ^F/χ^W_{PC} than LKA and LKB; this perhaps points to some unknown inhomogeneous structural feature particular to this material's processing or chemistry. This is a subject for future study.

V. DISCUSSION

A. Fracture mechanics model

Within the current model, T^F can only be estimated with knowledge of either χ^W or σ^F. The toughness of 2.0-, 1.5-, and 1.0-μm-thick LKA may then be calculated with the SEMATECH-supplied film stresses measured by wafer-curvature (Table I) and the values of T^F/χ^W_{PC} and σ^F/χ^W_{PC} from Table II. For 2.0-μm-thick LKA, $T^F = (0.091 \pm 0.014)$ MPa $m^{1/2}$; for 1.5-μm-thick LKA, $T^F = (0.089 \pm 0.014)$ MPa $m^{1/2}$; and for 1.0-μm-thick LKA, $T^F = (0.083 \pm 0.014)$ MPa $m^{1/2}$. All three values therefore agree within calculated uncertainties. The mean fracture toughness is a physically-reasonable number; the toughness of LKA is about 1/8 that of dense fused silica, as is the elastic modulus of this film.[34] For comparison, this is roughly the same fracture toughness as ice.[35]

In recent work by Quinn and Bradt, the one standard

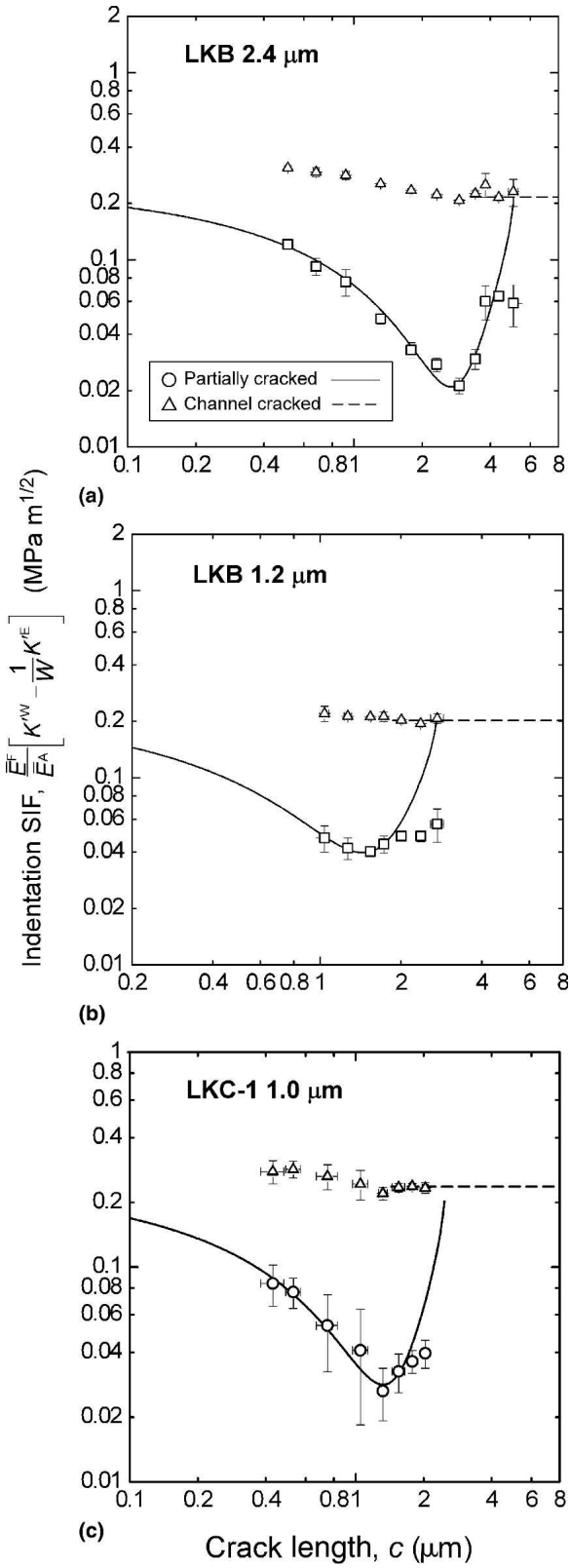

FIG. 10. Indentation stress-intensity factor for partially cracked films and channel-cracked films as a function of surface crack length for cube-corner fracture on (a) 2.4-μm-thick LKB, (b) 1.2-μm-thick LKB, and (c) 1.0-μm-thick LKC-1. Fits of the respective film fracture models for each set of data are shown.

deviation uncertainty of the micro-scale Vickers indentation fracture toughness test on a NIST Standard Reference Material for the fracture toughness of ceramics ranged from 2% to 6%.[36] This work also concluded that the Vickers fracture toughness test did not agree within experimental uncertainty with standard toughness measurement methods. Because the mechanism of crack propagation at cube-corner indentations is different from Vickers indentation (that is, the cube-corner mechanism is indentation wedging),[11] the Quinn and Bradt conclusion does not necessarily apply to the results here. It is acknowledged that the reliability of the indentation fracture measurement for very acute indenters is unknown and a subject for future study, if it is ever possible to fabricate and test standardized fracture specimens for low-κ films.

However, if the film stress is unknown, the critical thickness[37,38] (the maximum thickness of film that may be deposited before the film shatters under the influence of film stress) may be constructed from $T^{\mathrm{F}}/\chi_{\mathrm{PC}}^{\mathrm{W}}$ and $\sigma^{\mathrm{F}}/\chi_{\mathrm{PC}}^{\mathrm{W}}$. The condition for propagation of a channel crack through a blanket film under the influence of only the film stress is

$$T^{\mathrm{F}} = \psi_{\mathrm{CH}}\sigma^{\mathrm{F}}(t_{\mathrm{crit}}^{\mathrm{F}})^{1/2} \quad , \tag{19}$$

where $t_{\mathrm{crit}}^{\mathrm{F}}$ is the critical film thickness. $T^{\mathrm{F}}/\chi_{\mathrm{PC}}^{\mathrm{W}}$ and $\sigma^{\mathrm{F}}/\chi_{\mathrm{PC}}^{\mathrm{W}}$ can be combined with Eq. (19) to estimate $t_{\mathrm{crit}}^{\mathrm{F}}$ as

$$t_{\mathrm{crit}}^{\mathrm{F}} = \left[\frac{1}{\psi_{\mathrm{CH}}}\left(\frac{\chi_{\mathrm{PC}}^{\mathrm{W}}}{\sigma^{\mathrm{F}}}\right)\left(\frac{T}{\chi_{\mathrm{PC}}^{\mathrm{W}}}\right)\right]^2 \quad . \tag{20}$$

The only quantity in Eq. (20) that cannot be estimated from partially cracked film data is ψ_{CH}. $t_{\mathrm{crit}}^{\mathrm{F}}$ is not a material property, but it can be an important component engineering metric because it is a combination of both material properties and material configuration (the stress imposed on the material due to strain constraint by the substrate). Furthermore, estimation of the critical film thickness by a method other than actually depositing films of varying thickness may be better from a perspective of material comparison, especially if, as suggested here, film stress may be significantly higher for thinner films.

B. Simulation of fracture responses and model interpretation

The previous section showed that transformation of load, crack length, and apparent modulus data into fracture mechanics coordinates are a convenient way to analyze thin-film low-κ fracture data. However, more physical insight into the effects of changing material properties or configuration (stress or chemical changes by manufacturing processes), or of the phenomena asserted in creating the fracture model (such as substrate attenuation) can be gained by re-transforming the fracture mechanics model back to a *c*-*P* response.

Functional forms describing the way in which the contact dimension, a [for calculating SIFs, such as in Eqs. (4), (6), and (7)], and the substrate attenuation, $\bar{E}^{\mathrm{F}}/\bar{E}^{\mathrm{A}}$, vary with indentation load are needed to simulate the fracture responses. A simple way to do this is to assume that the apparent hardness is constant, and that $\bar{E}^{\mathrm{A}}$ is a single function of a/t^{F}, as was shown in Part I.[1] With the constant hardness assumption, $P^{1/2}$ is linear in a, and $\bar{E}^{\mathrm{F}}/\bar{E}^{\mathrm{A}}$ can be any empirical function of $P^{1/2}/(t^{\mathrm{F}}H^{\mathrm{F}^{1/2}})$. For simulation purposes in this work, the apparent hardness is always that estimated by Berkovich indentation. $\bar{E}^{\mathrm{F}}/\bar{E}^{\mathrm{A}}$ is simply represented as a second-order polynomial function of $P^{1/2}/(t^{\mathrm{F}}H^{\mathrm{F}^{1/2}})$ over the range of interest.

The fracture relationships of Eqs. (17) and (18) are complex with respect to crack length and indentation load, so extraction of the *c*-*P* response from the fracture mechanics description requires numerical solution. There are possibly multiple equilibrium solutions for a fixed indentation load, so the stability of the system must be invoked to find the physical solution. The fracture stability condition for an ideally brittle material is $\mathrm{d}K^{\mathrm{T}}/\mathrm{d}c < 0$, where $K^{\mathrm{T}} = K^{\mathrm{W}} + K^{\mathrm{E}} + K^{\mathrm{F}}$ is the sum of all stress-intensity factors. Figure 11 is plot of normalized SIF, K/T^{F} as a function of normalized crack depth, c'/t^{F} for a hypothetical indentation + film SIF fracture field. There are three possible crack lengths that satisfy the equilibrium condition, $K/T^{\mathrm{F}} = 1$. Clearly, however, the solution that must be chosen is the shortest crack that satisfies the equilibrium and stability conditions.

For a partially cracked film, the fracture stability criterion [with Eq. (17)] leads to the condition

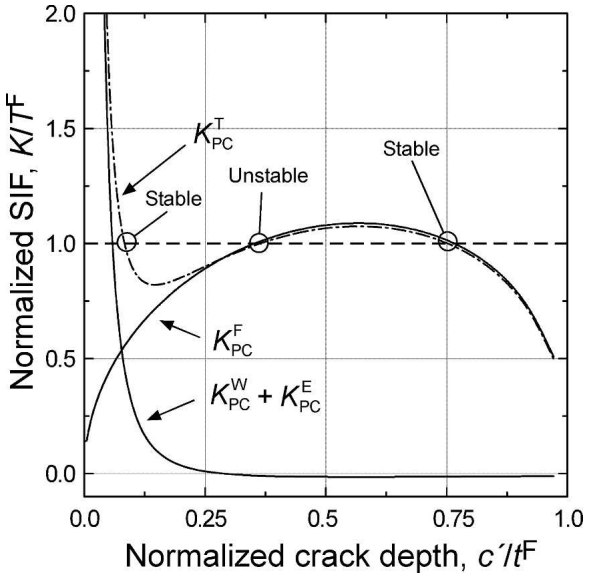

FIG. 11. Normalized SIF, K/T^{F} as a function of normalized crack depth, c'/t^{F} for a hypothetical indentation + film SIF fracture field. The shortest stable crack depth is the physically observed one.

$$\frac{dK_{PC}^{T}}{dc} = -\frac{3}{2c}\left[K_{PC}^{\prime W} - \frac{1}{W}K_{PC}^{E}\right] - \frac{1}{W}\frac{K_{PC}^{\prime W}}{c} - K_{PC}^{F}\left(\frac{1}{2c} - \frac{(1/2 - s)}{(1 - \ell c/t^{F})}\frac{\ell}{t^{F}}\right) < 0 \quad . \tag{21}$$

The *c*-*P* simulations for the partially cracked film were checked to make sure that Eq. (21) was always satisfied. The equilibrium channeling-cracked total SIF is always stable; the combination of the indentation SIFs is always stabilizing; and the channeling film-stress SIF is always neutral with respect to the surface crack length.

Figure 12(a) reproduces experimental *c*-*P* data for cube-corner indentation on 2.0-μm LKA. Also shown on Fig. 12(a) are the partially cracked (solid line) and channel-cracked (dashed line) simulations of the *c*-*P* response, using the T^{F}/χ_{PC}^{W} and σ^{F}/χ_{PC}^{W} values from Table II. Channel-cracking solutions are admitted only when the crack length is equal or greater to the film thickness; that is, the crack must be at least "square." The simulated fracture response reproduces the experimental data, but perhaps not as well as the fit in fracture mechanics coordinates, a possible artifact of the constant hardness assumption. However, the greatest experimental scatter in crack length—shown by the error bars of ±1 standard deviation—is in the region from 0.32 to 0.46 mN, the same region where the simulated *c*-*P* response is most sensitive to indentation load. Also in Fig. 12(a), crack-length simulations for film thicknesses of 1.5, 1.0, and 0.5 μm were generated by changing only the film thickness. No channel-cracking line appears for the thinner films because no channel-crack longer than the film thickness was possible. These simulations were generated by changing film thickness only; the apparent increases in film stress (Table II) were ignored so that the model behavior could be observed when film thickness was varied.

Figure 12(b) compares all experimental LKA cube-corner *c*-*P* data with simulations generated using the film stress values in Table II. When film stress is allowed to vary slightly from film to film, the simulation can reproduce features of the experimental *c*-*P* responses very well. Notably, the simulation can reproduce the invariance in crack length with respect to film thickness at indentation loads less than 0.4 mN; the one exception is the thinnest LKA film, 0.5 mm thick.

Figure 13 simulates the sensitivity of the fracture response to (a) changing the film toughness and (b) changing the film stress on the indentation fracture responses. In fact, they are difficult to distinguish; a 10% increase in film stress changes the fracture response nearly identically to a 10% reduction in fracture toughness, and vice versa. It was hoped at the outset of this work that an estimate of toughness could be made without an accompanying measurement of stress, but at this stage of development it does not seem possible. However, this does highlight the potential usefulness of t_{crit}^{F}, which accounts for stress and toughness, as a practical measure of a film's predilection to failure.

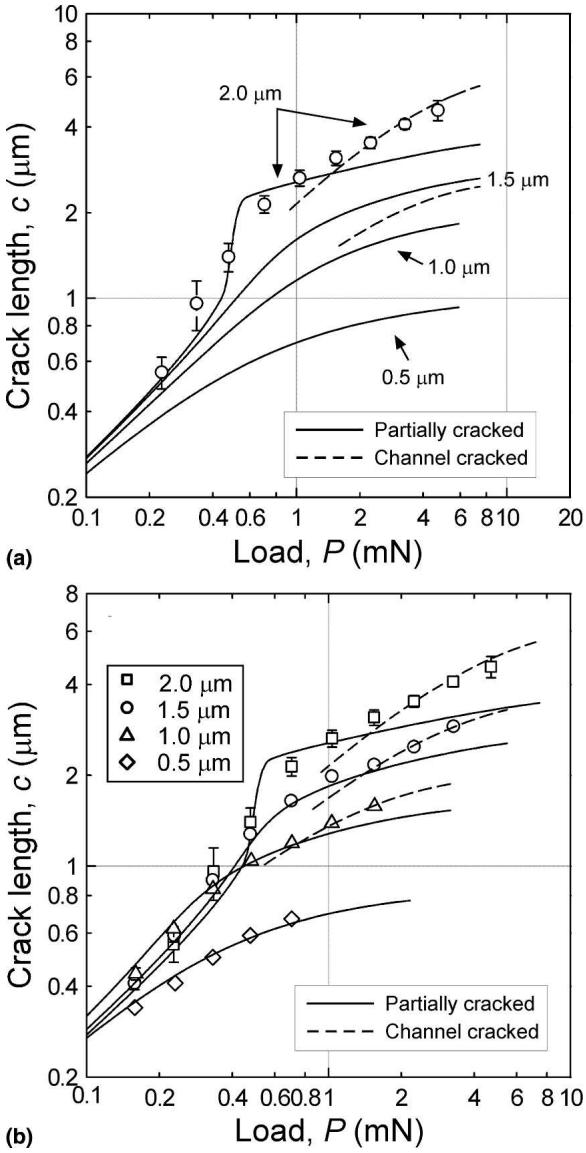

FIG. 12. Crack length versus indentation load simulations for cube-corner indentation on LKA. (a) The experimental *c*-*P* data for 2.0-μm LKA are shown and compared to the two-crack-shape film fracture model. Also shown are simulations of the film fracture response for 1.5-, 1.0-, and 0.5-μm films, generated by changing the film thickness in the simulation only. (b) Simulations of each LKA film thickness, where the film stress is allowed to individually match that extracted from the best fit of the fracture data (Figs. 9–11).

One of the central assumptions of the low-κ film fracture model is the existence of the substrate attenuation phenomenon, as outlined in Sec. II. The effect of substrate attenuation is to progressively dull the indentation SIFs as the substrate accommodates a larger fraction of

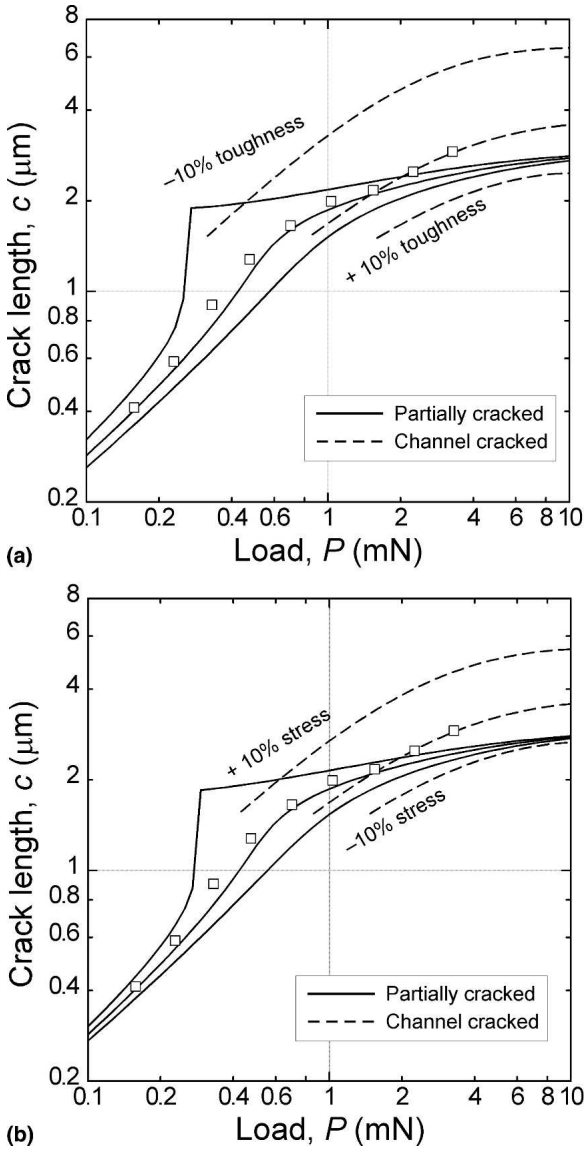

FIG. 13. Crack length versus indentation load simulation for cube-corner indentation on 1.5-μm LKA, with the effect of 10% changes in (a) toughness and (b) stress in the simulation.

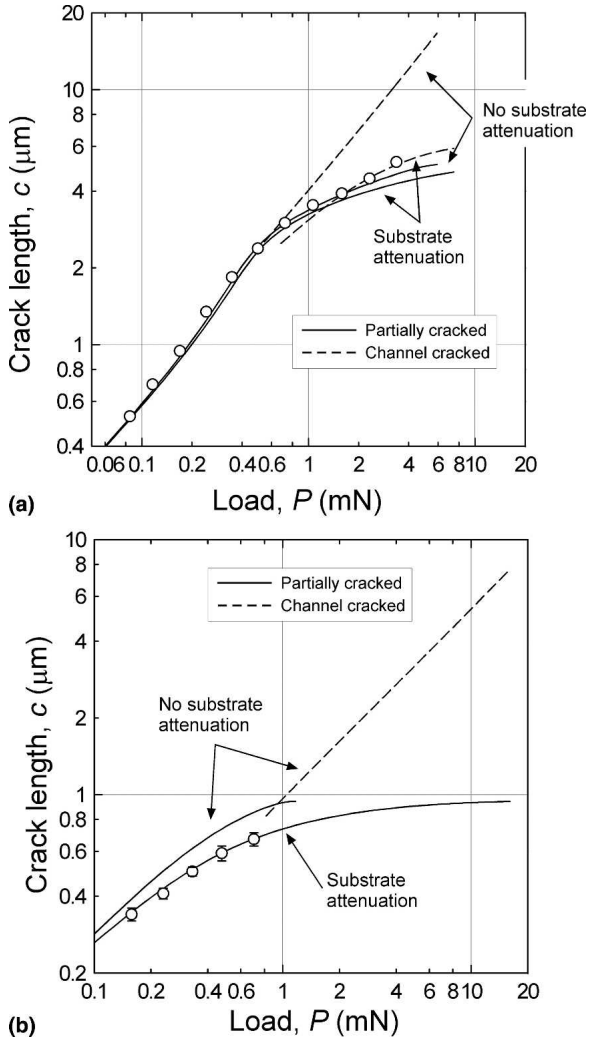

FIG. 14. Crack length versus indentation load simulation for cube-corner indentation, with and without substrate attenuation on (a) 2.4-μm LKB and (b) 0.5-μm LKA.

strain energy with increasing indenter penetration. Figure 14(a) shows simulations of the *c*-*P* response of a relatively thick film, 2.4-μm LKB, with and without the effect of substrate attenuation. Figure 14(b) is for a relatively thin film, 0.5-mm LKA. These will be used as illustrative examples.

Consider the simulated responses with and without substrate attenuation in Fig. 14(a). The partially cracked responses are almost identical, but the channel-cracked lines are different. Of course, at the smallest indentation loads, tensile film stress inflates the crack length to a value greater than it would be for a stress-free material. As seen in Fig. 5, the partially cracked film SIF quickly decreases to zero as the crack approaches the interface (that is, $c \rightarrow \ell t^{\mathrm{F}}$). By the time there is any significant substrate attenuation, the *c*-*P* response has already become insensitive to indentation load due to a rapidly decreasing $K_{\mathrm{PC}}^{\mathrm{F}}$ and the close approach of the crack to the interface. Once the channel crack is activated, the contribution of film stress to the fracture response increases to a level set by Eq. (14) and is invariant with further crack extension. Therefore, without substrate attenuation, scaling of the channel-cracked *c*-*P* response should resume at about $c \sim P^{2/3}$, as seen in the simulation without substrate attenuation. Indentation-driven channel cracking with substrate attenuation simulates the experimental fracture response much more realistically. The similarity between the late-stage partially cracked behavior and the strongly attenuated channel cracking might suggest that there is not, in fact, a change in crack shape. Without the crack-shape transition, however, the slight concave to convex transition of the *c*-*P* response at higher loads in the thicker films could not be reproduced [see at a load of

approximately 1.5 mN for 2.4-μm LKB, Fig. 14(a); see also at loads of 2.2 mN for 2.0-μm LKA and 1.5 mN for 1.5-μm LKA, Figs. 12 and 13 in Part I[1]]. An upward point of inflection in the *c-P* response when the crack length is greater than the film thickness is indicative of the transition to channel crack geometry.

Figure 14(a) plots *c-P* simulations with and without substrate attenuation for the thinnest film studied here, 0.5-μm LKA. As might be expected, a lack of substrate attenuation would result in longer crack lengths at fixed load. Furthermore, without substrate attenuation, a channel crack could be formed [that is, a solution of Eq. (18) is possible]. With even a generous estimate of $\omega = 0.4$ (see Table II), no channel crack can be formed with a cube-corner indenter when substrate attenuation is accounted for. The consequence for experimentalists is that thinner films are even more difficult to study than they might normally be with indentation fracture because the range of indentation loads over which radial fracture can be generated is shortened significantly by substrate attenuation. Indenters more acute than a cube corner could possibly be used to drive channel cracking in this particular film, if so desired.

VI. SUMMARY

A fracture and contact-mechanics based model for measurement of the fracture toughness of thin, low-dielectric constant films has been derived. This model combines the wedging mechanism of indentation radial fracture, the effect of substrate constraint on the indentation crack shape, the contribution of film stresses to the overall fracture response, and the influence of the substrate on the indentation stress fields. When all of these effects are accounted for, indentation fracture data for films of varying thickness and stress can be reconciled with one value of toughness for the material.

Pre-existing film stresses are considerable contributors to the overall fracture response. Prior results for the stress-intensity factors for a stressed, cracked thin film are extrapolated to the case of a low-Poisson's ratio, compliant film on a stiff substrate. It is shown that the distortion in the stress-intensity factor fields can be large if this is true. Furthermore, because the indentation cracks are contained within the film, the distribution of indentation strain energy between film and substrate must be taken into consideration. It is shown how the fraction of indentation strain energy contained in the film may be experimentally estimated by the apparent indentation modulus. Measurements of crack length and the indentation modulus at each indentation load can then be transformed into appropriate fracture mechanics coordinates for analysis.

If there is an independent measure of the film stress, the fracture toughness may be estimated. One organosilicate low-κ material was estimated to have a toughness of about 0.09 MPa $m^{1/2}$. If film stress is not known, then the critical film thickness for channel cracking may be estimated from the indentation fracture response. Simulation of film fracture responses shows that film stress, thickness, and toughness all play different and important roles when evaluating the indentation fracture response of these materials.

REFERENCES

1. D.J. Morris and R.F. Cook: Indentation fracture of low-dielectric constant films: Part I. Experiments and observations. *J. Mater. Res.* **23**(9), 2429 (2008).
2. D.J. Morris and R.F. Cook: Radial fracture during indentation by acute probes: I. Description by an indentation wedging model. *Int. J. Fract.* **136,** 237 (2005).
3. B.R. Lawn: *Fracture of Brittle Solids* (Cambridge University Press, Cambridge, UK, 1993).
4. G.R. Anstis, P. Chantikul, B.R. Lawn, and D.B. Marshall: A critical evaluation of indentation techniques for measuring fracture toughness. I. Direct crack measurements. *J. Am. Ceram. Soc.* **64,** 533 (1981).
5. D.M. Marsh: Plastic flow and fracture of glass. *Proc. R. Soc. London A* **282,** (1965).
6. A. Arora, D.B. Marshall, B.R. Lawn, and M.V. Swain: Indentation deformation/fracture of normal and anomalous glasses. *J. Non-Cryst. Solids* **31,** 415 (1979).
7. R.F. Cook and G.M. Pharr: Direct observation and analysis of indentation cracking in glasses and ceramics. *J. Am. Ceram. Soc.* **73,** 787 (1990).
8. D.J. Morris, S.B. Myers, and R.F. Cook: Sharp probes of varying acuity: Instrumented indentation and fracture behavior. *J. Mater. Res.* **19,** 165 (2004).
9. D.J. Morris, A.M. Vodnick, and R.F. Cook: Radial fracture during indentation by acute probes: II, Experimental observations of cube-corner and vickers indentation. *Int. J. Fract.* **136,** 265 (2005).
10. G.M. Pharr, D.S. Harding, and W.C. Oliver: Measurement of fracture toughness in thin films and small volumes using nano-indentation methods, in *Mechanical Properties and Deformation Behavior of Materials Having Ultra-Fine Microstructures,* edited by M. Nastasi, D.M. Parkin, and H. Gleiter (NATO ASI, Boston, MA, 1993) p. 449.
11. D.J. Morris and R.F. Cook: In situ cube-corner indentation of soda-lime glass and fused silica. *J. Am. Ceram. Soc.* **87,** 1494 (2004).
12. H. Tada, P.C. Paris, and G.R. Irwin: *The Stress Analysis of Cracks Handbook* (ASME Press, New York, 2000).
13. H. Gao, C-H. Chiu, and J. Lee: Elastic contact versus indentation modeling of multi-layered materials. *Int. J. Solids Struct.* **29,** 2471 (1992).
14. H. Xu and G.M. Pharr: An improved relation for the effective elastic compliance of a film/substrate system during indentation by a flat cylindrical punch. *Scr. Mater.* **55,** 315 (2006).
15. J. Mencik, D. Munz, E. Quandt, E.R. Weppelmann, and M.V. Swain: Determination of elastic modulus of thin layers using nanoindentation. *J. Mater. Res.* **12,** 2475 (1997).
16. H. Song, G.M. Pharr, and A. Rar: Assessment of new relation for the elastic compliance of a film-substrate system, in *Thin Films: Stresses and Mechanical Properties I*, edited by C.S. Ozkan, L.B. Freund, R.C. Cammarata, and H. Gao (Mater. Res. Soc. Symp. Proc. **695**, Warrendale, PA, 2002) p. 431.

17. J.L. Beuth: Cracking of thin bonded films in residual tension. *Int. J. Solids Struct.* **29,** 1657 (1992).
18. A.R. Zak and M.L. Williams: Crack point singularities at a bi-material interface. *J. Appl. Mech.* **30,** 142 (1963).
19. J.W. Hutchinson and Z. Suo: Mixed mode cracking in layered materials. *Adv. Appl. Mech.* **29,** 63 (1992).
20. J. Dundurs: Discussion of edge-bonded dissimilar orthogonal elastic wedges under normal and shear loading. *J. Appl. Mech.* **36,** 650 (1969).
21. J.J. Vlassak: Channel cracking in thin films on substrates of finite thickness. *Int. J. Fract.* **120,** 299 (2003).
22. T. Suga, G. Elssner, and S. Schmauder: Composite parameters and mechanical compatibility of material joints. *J. Compos. Mater.* **22,** 917 (1988).
23. B.N. Lucas, J.C. Hay, and W.C. Oliver: Using multidimensional contact experiments to determine Poisson's ratio. *J. Mater. Res.* **19,** 58 (2004).
24. B.N. Lucas, J.C. Hay, and W.C. Oliver: Using multi-dimensional contact mechanics experiments to measure Poisson's ratio of porous low-*k* films, in *Materials, Technology and Reliability for Advanced Interconnects and Low-k Dielectrics—2003*, edited by A.J. McKerrow, J. Leu, O. Kraft, and T. Kikkawa (Mater. Res. Soc. Symp. Proc. **766**, Warrendale, PA, 2003) p. 177.
25. K.E. Evans and A. Alderson: Auxetic materials: Functional materials and structures from lateral thinking! *Adv. Mater.* **12,** 617 (2000).
26. W. Yang, Z-M. Li, W. Shi, B-H. Xie, and M-B. Yang: Review on auxetic materials. *J. Mater. Sci.* **39,** 3269 (2004).
27. A. Alderson and K.E. Evans: Molecular origin of auxetic behavior in tetrahedral framework silicates. *Phys. Rev. Lett.* **89,** 2255031 (2002).
28. T.C.T. Ting and T. Chen: Poisson's ratio for anisotropic elastic materials can have no bounds. *Q. J. Mech. Appl. Math.* **58,** 73 (2005).
29. R.S. Lakes: Negative Poisson's ratio materials. *Science* **238,** 551 (1987).
30. G. Simmons and H. Wang: *Single Crystal Elastic Constants and Calculated Aggregate Properties: A Handbook* (MIT Press, Cambridge, MA, 1971).
31. T.Y. Tsui, A.J. McKerrow, and J.J. Vlassak: Constraint effects on thin film channel cracking behavior. *J. Mater. Res.* **20,** 2266 (2005).
32. T. Nakamura and S.M. Kamath: Three-dimensional effects in thin film fracture mechanics. *Mech. Mater.* **13,** 67 (1992).
33. J.M. Jacques, T.Y. Tsui, A.J. McKerrow, and R. Kraft: Environmental effects on crack characteristics for OSG materials, in *Thin Films—Stresses and Mechanical Properties XI*, edited by T.E. Buchheit, A.M. Minor, R. Spolenak, and K. Takashima (Mater. Res. Soc. Symp. Proc. **875**, Warrendale, PA, 2005). O10.6
34. S.M. Wiederhorn: Fracture surface energy of glass. *J. Am. Ceram. Soc.* **52,** 99 (1969).
35. J.J. Petrovic: Review: Mechanical properties of ice and snow. *J. Mater. Sci.* **38,** 1 (2003).
36. G.D. Quinn and R.C. Bradt: On the Vickers indentation fracture toughness test. *J. Am. Ceram. Soc.* **90,** 673 (2007).
37. A.A. Volinsky, J.B. Vella, and W.W. Gerberich: Fracture toughness, adhesion and mechanical properties of low-k dielectric thin films measured by nanoindentation. *Thin Solid Films* **429,** 201 (2003).
38. J.B. Vella, I.S. Adhihetty, K. Junker, and A.A. Volinsky: Mechanical properties and fracture toughness of organo-silicate glass (OSG) low-k dielectric thin films for microelectronic applications. *Int. J. Fract.* **120,** 487 (2003).